European Congress on Computational Methods in Applied Sciences and Engineering
ECCOMAS 2004
P. Neittaanmäki, T. Rossi, K. Majava, and O. Pironneau (eds.)
W. Rodi and P. Le Quéré (assoc. eds.)
Jyväskylä, 24–28 July 2004

LARGE EDDY SIMULATION OF A JET IN CROSSFLOW

Jochen Fröhlich*, Jordan A. Denev*, and Henning Bockhorn*

*Institute for Technical Chemistry and Polymer Chemistry, University of Karlsruhe,
Kaiserstrasse 12, 76128 Karlsruhe, Germany
e-mail: froehlich,denev,bockhorn@ict.uni-karlsruhe.de
web page: http://www.ict.uni-karlsruhe.de

Key words: jet in crossflow, large eddy simulation, mixing, vortex lines, PDF.

Abstract. *The paper presents large eddy simulations (LES) of a turbulent jet into a laminar crossflow. The velocity ratio is 3.3 and the Reynolds number 2100, based on the crossflow velocity. Inflow conditions for the jet were generated by an independent LES of a pipe flow. With the jet, a passive scalar is introduced which is computed as well. The results are validated against similar LES and experimental data. The instantaneous flow is visualized and related to findings in the literature. We propose to use vortex lines of the average flow in order to analyze the formation of the counter–rotating vortex pair. They reveal the dominant role of the hanging vortices near the jet exit but also show a contribution from deformed vortex rings to the jet vorticity. Furthermore, PDFs for the jet scalar are presented, which up to now were not computed for this case.*

1 INTRODUCTION

The configuration of a jet in crossflow (JICF) is an important prototype situation in fluid mechanics. Its many applications and variants range from aeronautical devices to configurations featuring discharge plumes, film cooling in turbo machinery or mixing in chemical engineering and combustion. An exhaustive review of related research is provided for example in [11].

Jet flows in general, exhibit pronounced instabilities and feature large–scale vortical structures. If the jet axis is not aligned with the surrounding mean flow an even more complicated interaction of different vortex systems in the instantaneous flow is generated [5]. For this reason the computation of a JICF by means of statistical turbulence models is a difficult task [10, 3]. Large eddy simulations (LES) or direct numerical simulations resolve a large part or even all of the turbulent motion resulting in a lower modelling error and substantially more information about the structure of the flow. Hence, several such studies have been undertaken in recent years for the JICF configuration [8, 19, 13].

The geometry of a JICF is displayed in Fig. 1. The principal physical parameters are the Reynolds number $Re = Re_\infty = U_\infty D/\nu$, defined with the free–stream velocity U_∞ and the jet diameter D, and the ratio $r = U_{jet}/U_\infty$ between the jet bulk velocity and the velocity of the cross flow. The ratio r allows to distinguish between weak jets that remain close to the wall, which is characteristic for film cooling applications in turbo machinery, and jets that intrude substantially into the cross flow. The latter regime occurs for $r > 1$ and is considered here. A further determining feature is the structure of the crossflow in terms of its average velocity profile and its turbulence level. The characteristics of the jet result from the upstream pipe flow and are fully characterized by the parameter $Re_{jet} = rRe_\infty$ if the flow in the pipe is fully developed.

In the present paper we report on LES for the JICF configuration focusing mainly on results concerning averaged values. A more detailed analysis of instantaneous features will be performed in future work.

2 COMPUTATIONAL SETUP AND NUMERICAL METHOD

The LES computations have been designed close to the ones in [19, 18] which, in turn, were configured in order to match with the experiments of [14]. Here, simulations are presented with $r = 3.3$ and $Re = 2100$ yielding a Reynolds number of 6930 in the pipe. The origin of the coordinate system is located in the center of the jet in the plane of the wall, $l_x = 2.7D$ downstream of the inlet section. The computational domain above the wall extends over a length $L_x = 13.7D$ in streamwise, $L_y = 8D$ in spanwise and $L_z = 12D$ in wall normal direction, as in [19], and is displayed in Fig. 1. The computational domain also covers the jet prior to the outlet over a distance of $l_z = 1D$. The inflow condition at $z = -D$ was generated within the simulation by simultaneously computing a pipe flow with periodic boundary conditions and an axial extent of $5D$. This length was selected to be the same as in the DNS computations of [4] at a bulk Reynolds number of 5300.

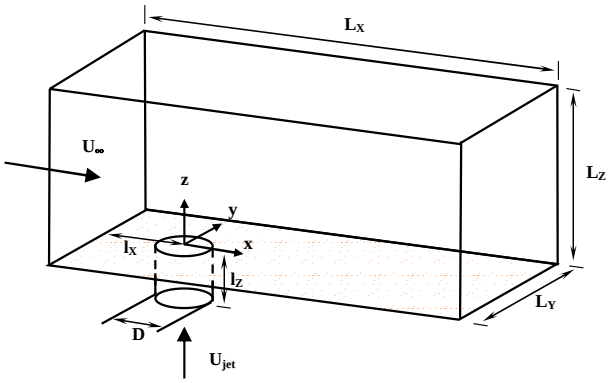

Figure 1: Sketch of the computational domain and nomenclature defining the geometry. Ratios L_x/D etc. are not to scale.

This length is on the save side since correlation lengths tend to decrease with Reynolds number. The crossflow was assumed to be laminar featuring a boundary layer with a thickness of $\delta_{99} = 0.5D$ which was implemented using a Blasius profile. It was checked in the results that the boundary along the wall remains laminar remote from the jet.

Together with the flow itself, the transport of a passive scalar S_1 was computed for which the boundary conditions were $S_1 = 1$ in the jet and $S_1 = 0$ in the crossflow together with homogeneous Neumann conditions on all other boundaries.

The simulations were performed with the code LESOCC2 [2, 7] employing a Finite Volume method of second order central differencing on block–structured curvilinear grids with collocated arrangement of variables to solve the Navier–Stokes equations for constant–density flow. It uses momentum interpolation to avoid pressure–velocity decoupling and a three–level Runge–Kutta scheme of second order for time stepping. The Smagorinsky model was employed for the representation of the unresolved fluctuations with $C_s = 0.1$ (RUN SM01) and $C_s = 0.2$ (RUN SM02) as well as the Dynamic Smagorinsky model (RUN DSM). If not stated otherwise, data from the first of these are reported. The unresolved scalar flux was represented by a turbulent diffusivity $\Gamma_t = \nu_t/Sc_t$ with a turbulent Schmidt number of $Sc_t = 0.6$. In order to conserve the bounds for the scalar, the non-oscillatory HLPA scheme of second order [20] is used. At solid walls, the Werner–Wengle wall function [17] was employed. It should however be noted that the near–wall grid, although not fully wall resolving, is relatively fine. The wall function therefore actually operates in the buffer layer, for which it is designed as well due to blending of the 1/7–power law with a linear law and integration of the velocity profile over the wall–adjacent cell. For the same reason van Driest damping near solid walls was applied to the eddy viscosity when computed in the Smagorinsky model.

The grid, without the periodic pipe, consists of about 1.5 Mio. cells and has been created with the grid generator ICEM–CFD–Hexa. It comprises 45 Blocks and contains

no hanging nodes. Typical cell sizes are $\Delta_z = 0.06D$ near the bottom wall as well as within the pipe, and $\Delta_r = 0.009D$ in radial direction at the pipe wall. Stretching ratios are below 1.03 in most parts of the domain except in lateral regions remote from the jet with large $|y|$. The shear velocity in the pipe has been computed to $u_\tau = 0.21U_\infty$ so that $\Delta_r^+ = 4$, with the data point in the cell center located 2 wall units remote from the wall, and $\Delta_z^+ = 26$. These spacings, in particular in $z-$direction, were chosen larger than in [19] in order to position a higher number of grid points in the jet itself. With $r = 3.3$, the jet is remote from the wall, as visible, in Fig. 2 below, so that a certain amount of wall modelling is possible without impacting on the computation of the jet. With the present grid $\Delta_z^+ = 5$ and hence $z_1^+ = 2.5$ for the wall–adjacent cell near the inflow boundary. The streamwise and spanwise resolution is also high, with $\Delta_x = 0.06D$ and $\Delta_y = 0.06D$ being typical values upstream of the jet exit, respectively. With this relatively high resolution the amount of modelling introduced by the wall function approach is very small.

3 RESULTS

3.1 Average flow

Let us first discuss the average flow and the different regions it exhibits. Fig. 2a presents a plot of average streamlines and average concentration in the centerplane. The trajectory of the jet and its bending into the direction of the crossflow is clearly visible. Behind the jet, a saddle point appears as a result of the fluid being fed into this plane from the transverse direction. Recirculation is strongest in the plane $z = 0.5D$. Also, a pronounced upward motion can be observed in the rear of the jet. Fig. 2b shows the streamlines close to the bottom wall in the plane $z = 0.03D$. Further away from the wall at $z = 0.5D$, the usual pattern of a recirculation region is observed with a vortex pair and a saddle point at its rear end, here around $x = 1.8D$, and converging streamlines downstream of it (Fig. 2c). This picture is in agreement with the analysis of experimental data in [9].

A central feature of the average flow is the counter–rotating vortex pair (CVP) in the interiour of the jet which is displayed in Fig. 2d and 2e oriented normal to the mean flow. The resulting transport of the scalar generates a kidney–shaped average concentration field. Note that the focus of the streamlines in the early stages is not identical with the concentration maximum (Fig. 2d). Higher coincidence is only observed further downstream as revealed by Fig. 2e. The spiraling of streamlines in the interiour of the jet visible in these plots reflects the deceleration of the jet in streamwise direction. These graphs also show secondary vortices near the ground plate. The whole pattern is termed an 'owl face of the second kind' in [12] as it exhibits two vortex pairs. The near-wall secondary vortices grow with streamwise distance until they attain a limiting width as visualized by the wall–streamlines in Fig. 2b. This pattern in fact corresponds nicely to the related wall–streamline pattern suggested for this case in [12].

The vertical jet constitutes an obstacle for the crossflow and as a result produces a recirculation in the rear. Hence, it is legitimate to compare this flow to the one around a solid cylinder mounted on a ground plate [5]. In [6] this flow was investigated with a height–to–diameter ratio of $H/D = 2.5$ with a very thin approaching boundary layer as in the present case. A fundamental difference between both configurations is introduced through the upward entrainment of fluid by the jet. This produces a strong upward motion in the wake around the centerplane (Fig. 2a) and a corresponding sense of rotation of the vortices displayed in Fig. 2d and Fig. 2e. A true obstacle as a solid cylinder of finite height in a thin boundary layer produces a downward motion in the rear and hence trailing vortices with the opposite sense of rotation [6] so that the flow impinges on the ground plate without creating secondary vortices and yields a simpler pattern of wall streamlines with just one vortex pair.

3.2 Statistical data and validation against reference run

Figure 3 and 4 display statistical data on vertical cuts in the centerplane where reference data are available (throughout, averaged values are denoted by angular brackets). Comparison is possible with LES of Yuan et al. [19, 18] who have performed very similar computations employing a dynamic mixed model (Case 3 II in [19]). The symbols represent experimental data by Sherif and Pletcher [14] to which Yuan et al. referred to when setting up their computations. In [19] these data are discussed and it is conjectured that in the experiment transition to turbulence has actually taken place near the ground plate. Also, the jet apparently exhibited slightly different characteristics so that these authors, in order to match the experimental data, chose a lower Reynolds number as in the experiment conducted with $r = 4, Re = 4820$. Hence, the LES data of [19, 18] obtained under the same conditions should match with the present results – with deviations resulting from different grids, physical as well as numerical modelling – while the agreement with the experimental data is subject to slight differences in the respective conditions and should not be over–interpreted. This applies in particular to the near–wall region. In Fig. 3a, the average velocity magnitude U_m is plotted instead of a single component in order to allow comparison with the hot wire measurements mimicking the insensitivity of this device with respect to the direction of the flow [19] (U_m was computed in RUN SM01 only). Fig. 3b displays the corresponding fluctuations. The present results in both graphs correspond very well with the LES reference data. In the far field, they are a little closer to the experiments but to a small extent only.

The average scalar concentration is shown in Fig. 4a. In the early stages at $x = 1.84D$ some discrepancy is observed. The present data exhibit a maximum closer to the wall compared to the experimental ones while those of the LES in [18] have their maximum slightly above. Computations under the same conditions with different subgrid–scale models in the momentum equation, impacting on the modelling in the scalar equation via the turbulent Schmidt number, have been performed and are reported as well. The average eddy viscosity in RUN SM01 is such that in the centerplane its maximum is 1.5ν

which is attained around $x = 1.5D, z = 3D$. The larger eddy viscosity introduced in the latter runs reduces the height of the jet by a small amount but leaves the solution at this station fairly unchanged. This difference might result from the different subgrid–scale models employed. In [18], a dynamic mixed model was used for the scalar concentration while here we employed pure eddy–viscosity models. Further downstream, the present data match the reference LES and experiments well. Similar observations can be made concerning the fluctuations of the scalar reported in Fig. 4b.

3.3 Instantaneous flow

The instantaneous flow exhibits particular vortex structures in different regions which are displayed in Fig. 5. For the near field close to the outlet, the most important coherent structures are the spanwise rollers generated in the shear layer at the windward face of the jet. Note that these turn in counterclockwise sense, i.e. the vorticity vector points into the negative $y-$direction. The spanwise rollers interact with the vertical vortices starting at the rear face of the jet outlet at about 45° from the centerplane (see Fig. 2c) and extending upwards. In [19] a thorough analysis of the instantaneous structures under the present conditions has been performed. Here, we will not enter into the details of this discussion since the interaction of the different vortex systems is extremely complex and still subject to debate in the literature.

Figure 5b displays an iso–surface of the concentration S_1 at the same instant as used for the pressure fluctuations in Fig. 5a. It is obvious how the large–scale vortical structures entrain fluid from the jet forming pockets of higher concentration. This is particularly visible at the windward face of the jet. Further downstream, the concentration field is even more perturbed so that large isolated pockets are formed as visible in this figure around $x = 5D$.

In Fig. 5a vertical vortex structures are also visible near the bottom plate around $x = 5D$. In order to study the wake structure behind the JICF we introduced a second scalar S_2 in the computations with boundary condition $S_2 = 1$ in the crossflow boundary layer, i.e. up to a wall distance of $0.5D$. For $z > 0.5D$ as well as in the jet inlet S_2 was set to zero. The same boundary conditions as for S_1 were applied at all other boundaries. This approach is similar to the visualizations in [5] where a smoke wire was introduced close to the bottom wall upstream of the jet. The thickness of the boundary layer was smaller and the Reynolds number higher in these experiments but in particular for $r = 4$ wake vortices were clearly visible over a substantial distance from the wall. Figure 5a shows that behind the jet, near–wall fluid is entrained upwards in organized motion. More precisely, this takes place in the cores of vertical vortices forming an alternating vortex street similar to the von Karman alley. This is visualized in Fig. 5b by means of an instantaneous iso–surface of S_2 viewed from above. As discussed in [9], the flow in the rear of a JICF differs from the one behind a solid cylinder as it does not exhibit substantial momentum deficit. The present results on one hand feature a recirculation zone immediately behind the jet (Fig. 2c) but the velocity deficit is rapidly attenuated. At

$(x/D, y/D, z/D) = (3.2, 0, 1)$ the average streamwise velocity in the centerplane again has reached the free stream velocity, whereas behind a solid cylinder it remains substantially below this value even very far downstream.

4 Analysis of the average flow by means of the vorticity

In the literature on the subject, the origin of the CVP is debated controversially. Some authors suggest that its origin is the deformation of ring vortices which would appear in a straight jet without crossflow [1, 9]. Others suggest that the origin is to be found in the hanging vortices at the rear end of the jet (Fig. 2c) [19]. To address this issue, we analyze the average vorticity field by means of vortex lines. As any other vector field, vorticity can be displayed by a vector plot but also by means of lines tangential to these vectors, like streamlines are used for the velocity vectors. In [16], such vortex lines resulting from computations with a statistical model were presented for $r = 2, 4, 8$ but with a symmetry condition at the lower boundary instead of a solid wall inducing a boundary layer.

Fig. 7 reports vortex lines for the average flow obtained from the present computations as coloured tubes with the colour representing the vorticity magnitude. Note that these vortex lines do not in general represent the cores of vortices nor a particular concentration of vorticity. To relate them to the velocity field five selected streamlines starting in the jet outlet are plotted as red lines. The three of them starting in the centerplane remain in this plane for symmetry reasons. The two starting at $x = 0, y = \pm 0.5$ first move outward, then upwards and inwards due to the CVP. The black spirals are streamlines in planes perpendicular to the $x-$axis as displayed in Fig. 2d and e. The vortex lines were started in one of the two foci and then computed over a certain distance by the graphics software. Hence, in addition to the results in [16] we can address the relation of the vortex lines to the CVP. Since the symmetry of the average flow field is not perfect because of the finite averaging time and due to offsets in the starting point, the vortex lines tend to spiral without forming closed loops, as visible in Fig. 7a.

The following observations can be made. First of all, there is not a single vorticity line connecting all foci in the planes $x = const.$ with each other as might be expected. When starting a vorticity line in a focus of the two–dimensional streamlines (black) two cases can be distinguished. In the upper pictures, the vortex line passes through the windward face of the jets where the shear layer creates substantial vorticity. This happens for starting points in planes close to the jet outlet. These lines can become quite straight further downstream and towards their end exhibit an upward trend. Nevertheless, they remain below the average jet streamlines at the downstream end. Their patterns are hence topologically equivalent to deformed vortex rings surrounding the jet outlet : the observed patterns can be obtained by starting from a circular vortex ring around the jet at a certain height by lifting its rear part according to the average velocity which is directed upwards behind the jet. The deformation, in particular in Fig. 7a is such that a portion of this deformed vortex ring constitutes the vorticity close to the centers of the CVP. On the other hand, there also exist vortex lines which connect the interiour of the CVP to the

bottom, as visible in Fig. 7c and d. These lines were generated starting the integration in the foci further downstream. In both graphs, the vortex lines exhibits a similar shape with the line in the latter remaining below and rear of the one in Fig. 7c. The horizontal ends of the vortex line in Fig. 7d reflect the presence of the thin wall boundary layer. It prevents vortex lines from ending flush to the bottom boundary which would be the case with a no–slip conditions. Fig. 7c is particularly important as it shows that strong vertical vorticity near the jet outlet on the lateral borders is converted into streamwise vorticity by the action of the crossflow thus contributing to the vorticity in the CVP. The beginning of this vortex lines marks the steady 'hanging vortex' identified in [19]. This line is created by the crossflow and, also by the crossflow, is bent towards the rear of the jet thus inducing an upward vertical motion in the near wake. It does however not constitute the center of the CVP but near the jet remains closer to the centerplane and only later happens to touch its core. As a consequence of the upward motion, the vorticity lines which would form circles around the outlet without the presence of crossflow at the jet exit are distorted by this upward motion as visible in Fig. 7b and Fig. 7a. This distortion aligns them with the CVP in this manner also contributing to its magnitude. From this analysis we conclude that the hanging vortices form a central ingredient to the formation of the CVP. The deformation of vortex rings and the vorticity generated in the windward face of the jet, however, also is an important mechanism contributing to the CVP in the direct vicinity of the outlet. The average vorticity field in fact seems to be substantially more complicated than suggested by the plots in [16].

4.1 Analysis of PDFs

Time signals were recorded at selected points of the flow field for about $100t_\infty$ with $t_\infty = D/U_\infty$. These were used to generate probability density functions (PDF) of the scalar S_1 in order to characterize the mixing. Such data was not reported in [18]. Typical results are displayed in Fig. 8 and 9.

In Fig. 8, data from points along the central velocity trajectory of the jet are reported. They can be related to the results for $\langle S_1 \rangle$ and $\langle S_1' S_1' \rangle$ in Fig. 4. Close to the outlet, the jet fluid prevails (point 1) but very soon a substantial portion of ambient fluid is present even in the very center of the jet. At points 2 to 4 a substantial variance is observed which is generated by the intermittency of the flow. Further downstream, the permanent mixing reduces the fluctuations and yields a narrow PDF. Intermittency with intrusion of ambient fluid is still present as revealed by the PDF for $S_1 \approx 0$. It can also be observed that the computed PDF becomes less smooth for points further downstream. This is a consequence of the lower velocity, larger structures and hence less vortex events to average over.

Fig. 9 provides a complementary picture presenting PDFs remote from the central trajectory in a plane normal to the mean flow at $x = 5.54$. Point 1 in this figure is located at the lateral border of the jet. Here, the PDF is almost constant over the range $S_1 = 0.02 \ldots 0.22$ with an additional peak at $S_1 = 0$. At point 2, mixing generates a

relatively narrow Gauss—shaped PDF, but at point 3 this shape is much more slanted towards low values due to the convection of ambient fluid into the jet by the CVP. Points 6 and 10 are located at the lower and upper border of the jet, respectively. Again due to the CVP, a substantial asymmetry between both is observed since at point 6 the velocity is directed into the jet. At point 10, substantial intermittency is observed between ambient and jet fluid.

The PDFs at points 7, 8, 9 in the interiour of the jet all assume a maximum around $S_1 = 0.2$, also observed at point 10. In [15] this behaviour is termed a 'non–marching' PDF and has been observed for a jet with $r = 5$ at $Re = 3320$. In contrast to jets with higher values of r, for $r = 5$ this did not change when going from the near field of the jet to the far field. The transition point, according to these authors, is located at $s_{crit} = 0.3r^2D$ where s is the coordinate along the central trajectory. The present value $r = 3.3$ yields $s_{crit} = 3.27$ so that according to this definition the plane at $x = 5.54$ is located in the far field. The same non–marching behaviour was also observed in PDFs from the present simulations at $x = 1.87$ (not shown here). The present data hence support the findings of [15] for the case $r = 3.3$ and lower Reynolds number. In general, many PDFs computed exhibit a high degree of intermittency, as visible through the peaks near the left interval boundary. The shapes do only very roughly correspond to clipped Gaussians but in particular at the lateral border exibit a more complicated shape.

5 Conclusions

Large eddy simulations of a jet in crossflow have been performed including the scalar transport and mixing of the jet fluid with the ambient flow. For analysis of the interaction between the near–wall flow and the jet in the wake region a second scalar was introduced. This indeed proved to be helpful when analysing the instantaneous flow structure and will be exploited further in later analysis. The data reported here concern to a large extent average quantities. In particular, average velocity and jet scalar have been analyzed together with the related average fluctuations. The results show close agreement with experimental and numerical data from other authors [14, 19, 18].

Vortex lines were determined for the average flow which up to now were almost not considered in previous references. It was found that they provide helpful information on the generation of the counter–rotating vortex pair which is discussed controversely in the literature. We found that the hanging vortices form a central ingredient to the formation of the CVP. Deformed vortex rings, the rear part of which is lifted by the upward velocity behind the jet, also contribute to the vorticity of the CVP.

Finally, PDFs of the jet scalar, not reported in [18], were determined from timesignals at selected points. The PDFs at cross sections $x = 1.83$ and $x = 5.54$ are found to be of the 'non–marching' type which agrees with the experiments of [15]. In future work, the unsteady features of the timesignals will be analyzed in more detail to investigate the role of coherent structures in this flow.

Acknowledgments

This work was supported by the German Research Foundation DFG through the priority programmes SPP 1141 (`www.ifv.uni-hannover.de/spp-mischen`) and SFB 606 (`www.sfb606.uni-karlsruhe.de`) which is greatfully acknowledged. Dr. J. Wissink kindly provided the implementation of the Blasius profile.

REFERENCES

[1] J. Andreopoulos. On the structure of jets in a crossflow. *J. Fluid Mech.*, 157:163–197, 1985.

[2] M. Breuer and W. Rodi. Large eddy simulation of complex turbulent flows of practical interest. In E.H. Hirschel, editor, *Flow simulation with high performance computers II*, volume 52 of *Notes on Numerical Fluid Mechanics*, pages 258–274. Vieweg, Braunschweig, 1996.

[3] A.O. Demuren. Characteristics of three–dimensional turbulent jets in crossflow. *Int. J. Engrg. Sci.*, 31:899–913, 1993.

[4] J.G.M. Eggels, F. Unger, M.H. Weiss, J. Westerweel, R.J. Adrian, R. Friedrich, and F.T.M. Nieuwstadt. Fully developed pipe flow: a comparison between direct numerical simulation and experiment. *J. Fluid Mech.*, 268:175–209, 1994.

[5] T.F. Fric and A. Roshko. Vortical structure in the wake of a transverse jet. *J. Fluid Mech.*, 279:1–47, 1994.

[6] J. Fröhlich and W. Rodi. LES of the flow around a cylinder of finite height. In N. Kasagi, J.K. Eaton, R. Friedrich, J.A.C. Humphrey, M.A. Leschziner, and T. Miyauchi, editors, *Proceedings of 3rd Int. Symp. on Turbulence and Shear Flow Phenomena, Sendai, Japan, 25.-27.6.2003*, volume III, pages 899–904, 2003, to appear in Int. J. Heat Fluid Flow.

[7] C. Hinterberger. *Dreidimensionale und tiefengemittelte Large–Eddy–Simulation von Flachwasserströmungen.* PhD thesis, Institute for Hydromechanics, University of Karlsruhe, 2004.

[8] W.P. Jones and M. Wille. Large-eddy simulation of a plane jet in a cross flow. *Int. J. Heat and Fluid Flow*, 17:296–306, 1996.

[9] R.M. Kelso, T.T. Lim, and A.E. Perry. An experimental study of round jets in cross–flow. *J. Fluid Mech.*, 306:111–144, 1996.

[10] S.W. Kim and T.J. Benson. Calculation of a circular jet in crossflow with a multiple–time–scale turbulence model. *Int. J. Heat Mass Transfer*, 35:2357–2365, 1992.

[11] R.J. Margason. 50 years of jet in cross flow research. *Computational and experimental assessment of jets in crossflow*, pages 1.1–1.41, 1993. AGARD-CP-534.

[12] A.E. Perry and H. Hornung. Some aspects of three–dimensional separation, part II: Vortex skeletons. *Z. Flugwiss. Weltraumforsch.*, 8:155–160, 1984.

[13] J.U. Schlüter and T. Schönfeld. LES of jets in cross flow and its application to a gas turbine burner. *Flow, Turbulence and Combustion*, 65:177–203, 2000.

[14] S.A. Sherif and R.H. Pletcher. Measurements of the flow and turbulence characteristics of round jets in cross flow. *J. Fluids Eng*, 111:165, 1989.

[15] S.H. Smith and M.G. Mungal. Mixing, sturcutre and scaling of the jet in crossflow. *J. Fluid Mech.*, 357:83–122, 1998.

[16] R.I. Sykes, W.S. Lewellen, and S.F. Parker. On the vorticity dynamics of a turbulent jet in a crossflow. *J. Fluid Mech.*, 168:393–413, 1986.

[17] H. Werner and H. Wengle. Large–Eddy Simulation of turbulent flow over and around a cube in a plane channel. In F. Durst, R. Friedrich, B.E. Launder, F.W. Schmidt, U. Schumann, and J.H. Whitelaw, editors, *Selected Papers from the 8th Symposium on Turbulent Shear Flows*, pages 155–168. Springer, 1993.

[18] L.L. Yuan and R. L. Street. Trajectory and entrainment of a round jet in crossflow. *Phys. Fluids*, 10(9):2323–2335, 1998.

[19] L.L. Yuan, R.L. Street, and J.H. Ferziger. Large–eddy simulations of a round jet in crossflow. *J. Fluid Mech.*, 379:71–104, 1999.

[20] J. Zhu. A low–diffusive and ocillation–free convection scheme. *Comm. Appl. Numer. Meth.*, 7:225–232, 1991.

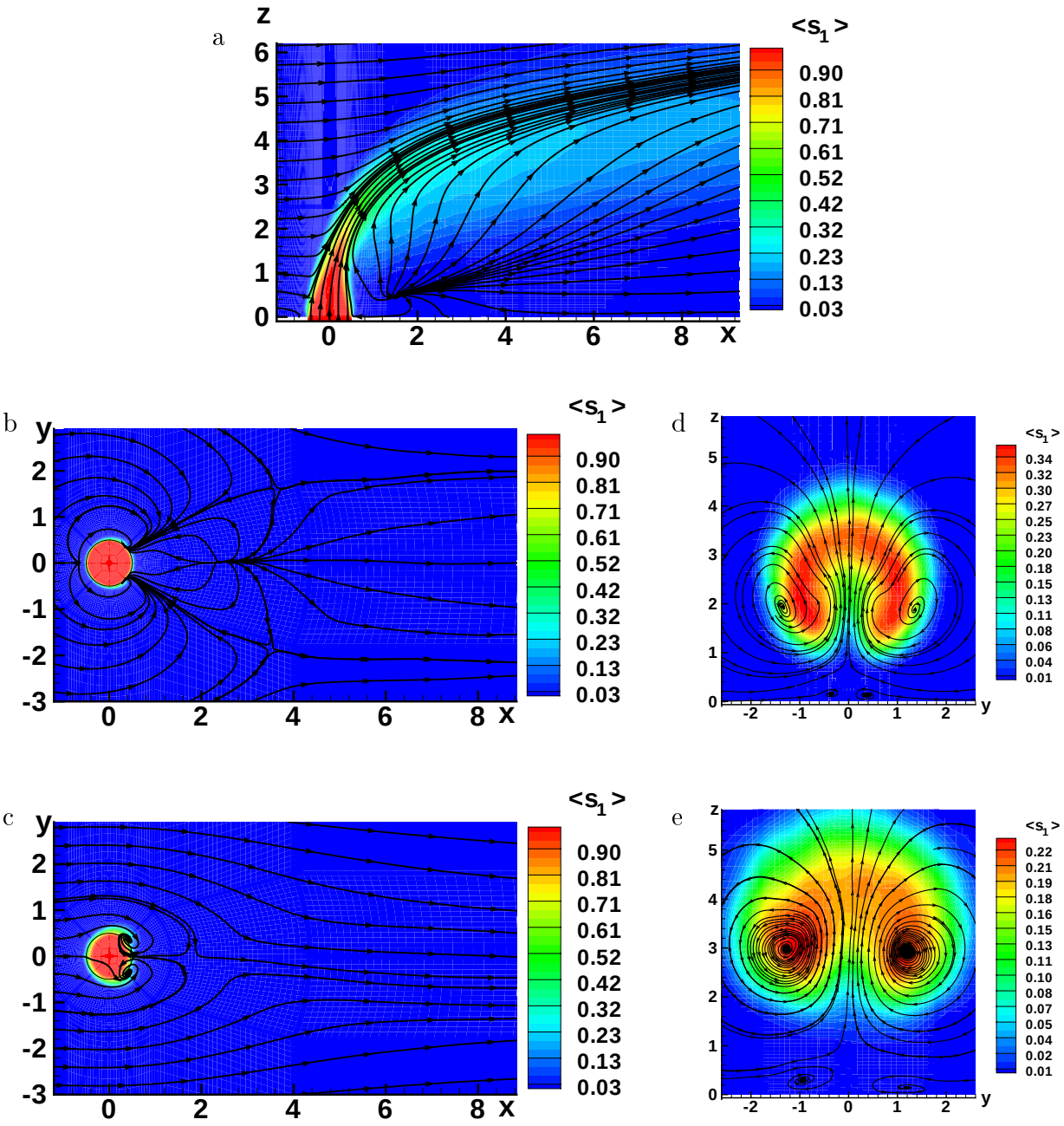

Figure 2: Average streamlines in black and average concentration as colour scale in different planes. a) centerplane $y = 0$, b) wall parallel plane at $z = 0.03D$, c) wall parallel plane at $z = 0.5D$, d) plane normal to the flow at $x = 1.83D$, e) plane normal to the flow at $x = 5.54D$. The plots do not display the entire domain but appropriate zooms around the jet.

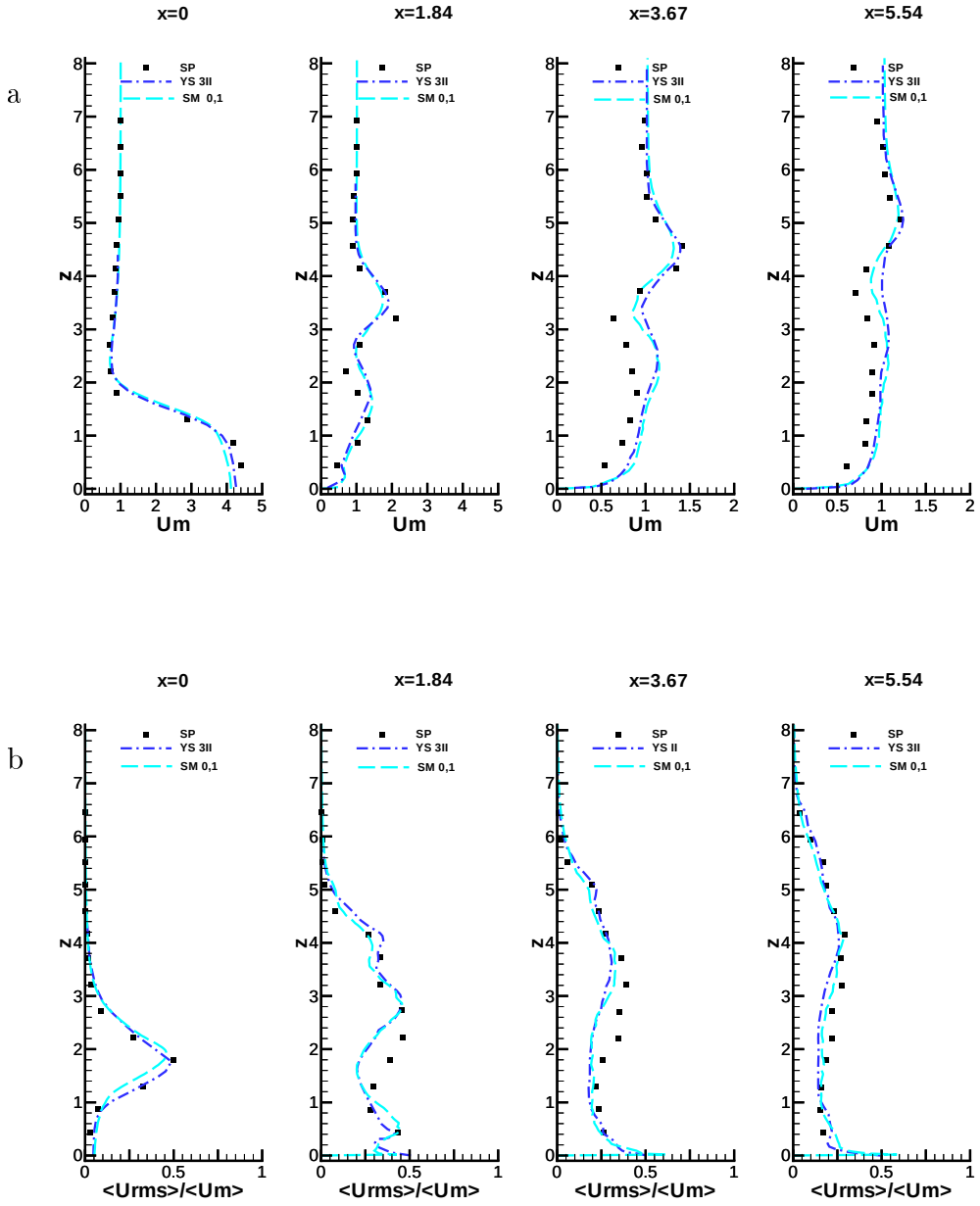

Figure 3: Statistical data along cuts in the centerplane at different streamwise positions $x = 0$, $x = 1.84D$, $x = 3.67D$, $x = 5.54D$. a) Average velocity magnitude $U_m = \langle\sqrt{u^2 + v^2 + w^2}\rangle$, b) corresponding fluctuations of velocity magnitude. Symbols are data from [14], line styles are: $-\cdot-$ data from [19] and [18], $--$ SM 0.1, $\cdots$ SM 0.2, ——— DSM.

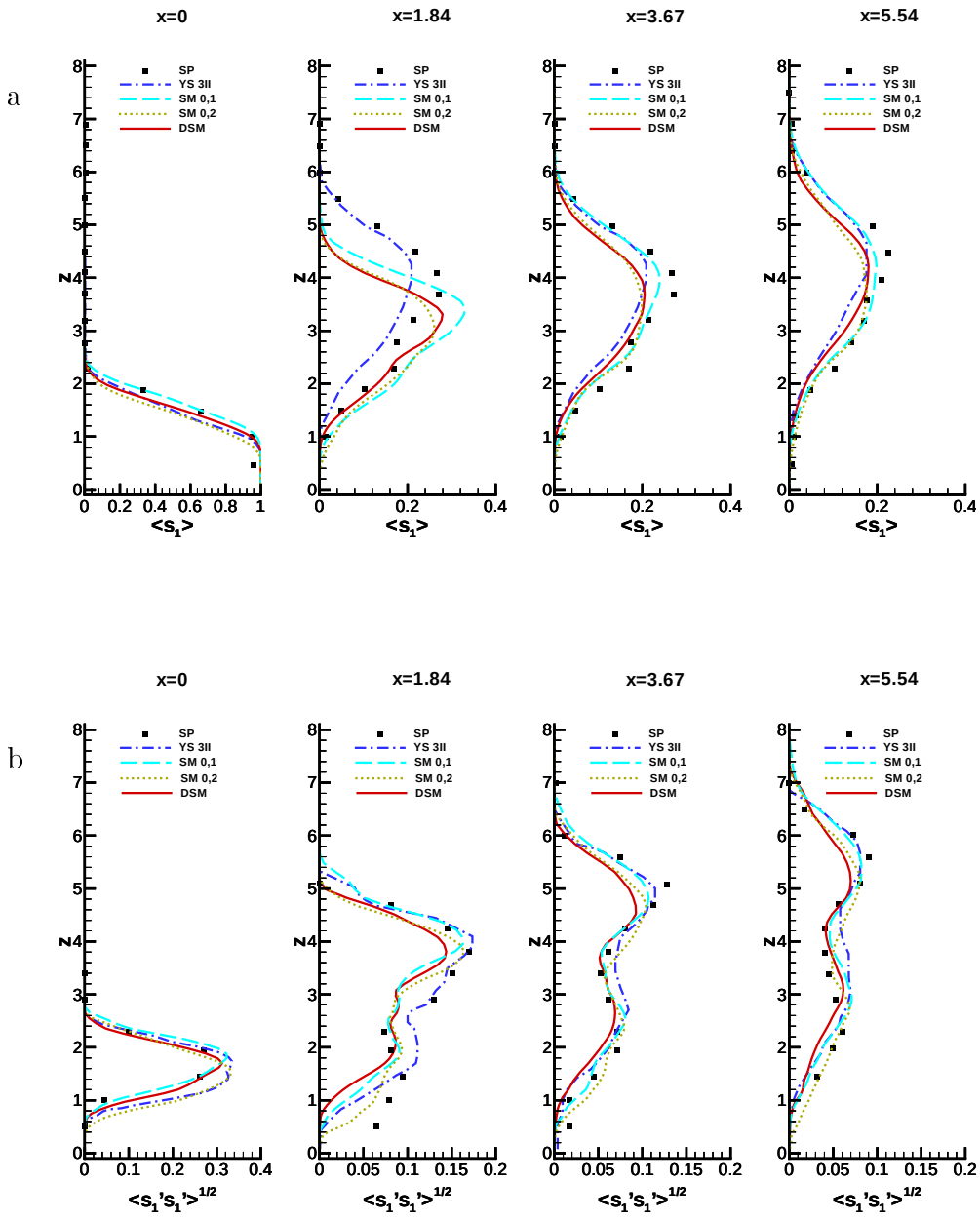

Figure 4: Statistical data along cuts in the centerplane at different streamwise positions $x = 0$, $x = 1.84D$, $x = 3.67D$, $x = 5.54D$. a) average scalar concentration, b) scalar fluctuations. Symbols are data from [14], line styles are: $-\cdot-$ data from [19] and [18], $--$ SM 0.1, $\cdots$ SM 0.2, ——— DSM.

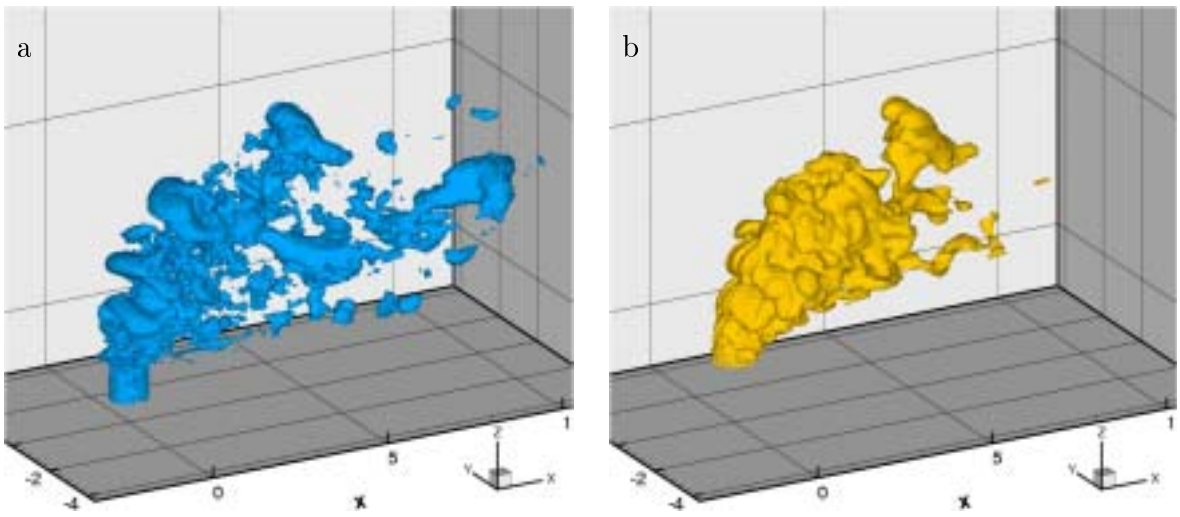

Figure 5: Three–dimensional views of flow field and scalar. a) Surface of instantaneous pressure fluctuation $p - \langle p \rangle = 0.1$ for RUN SM01. b) Instantaneous iso–surface of concentration $S_1 = 0.25$ in this run at the same instant.

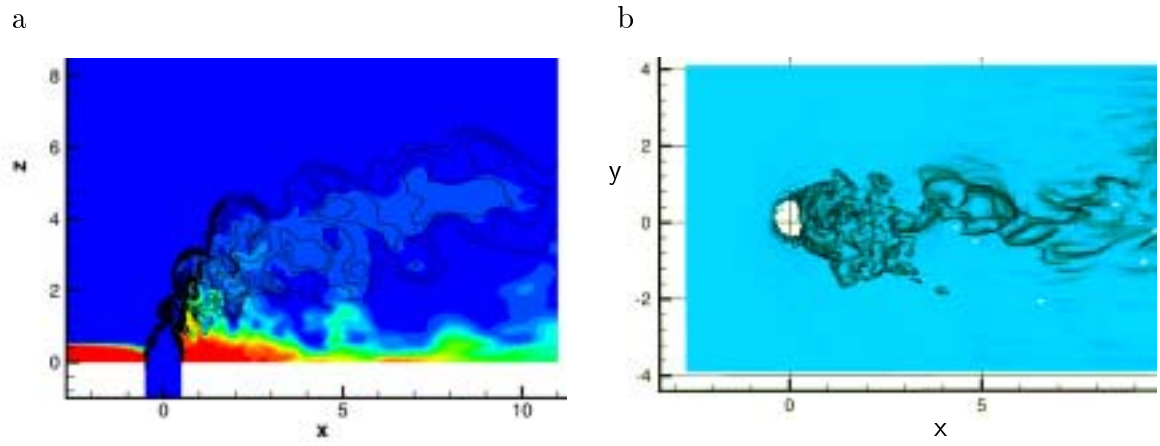

Figure 6: Instantaneous plots of the scalar S_2 introduced near the bottom plate. a) Contour plot in the centerline with S_2 represented by the colour plot and S_1 by the contour lines, both ranges are from 0 to 1. b) Instantaneous iso–surface of concentration $S_2 = 0.15$ viewed from the top.

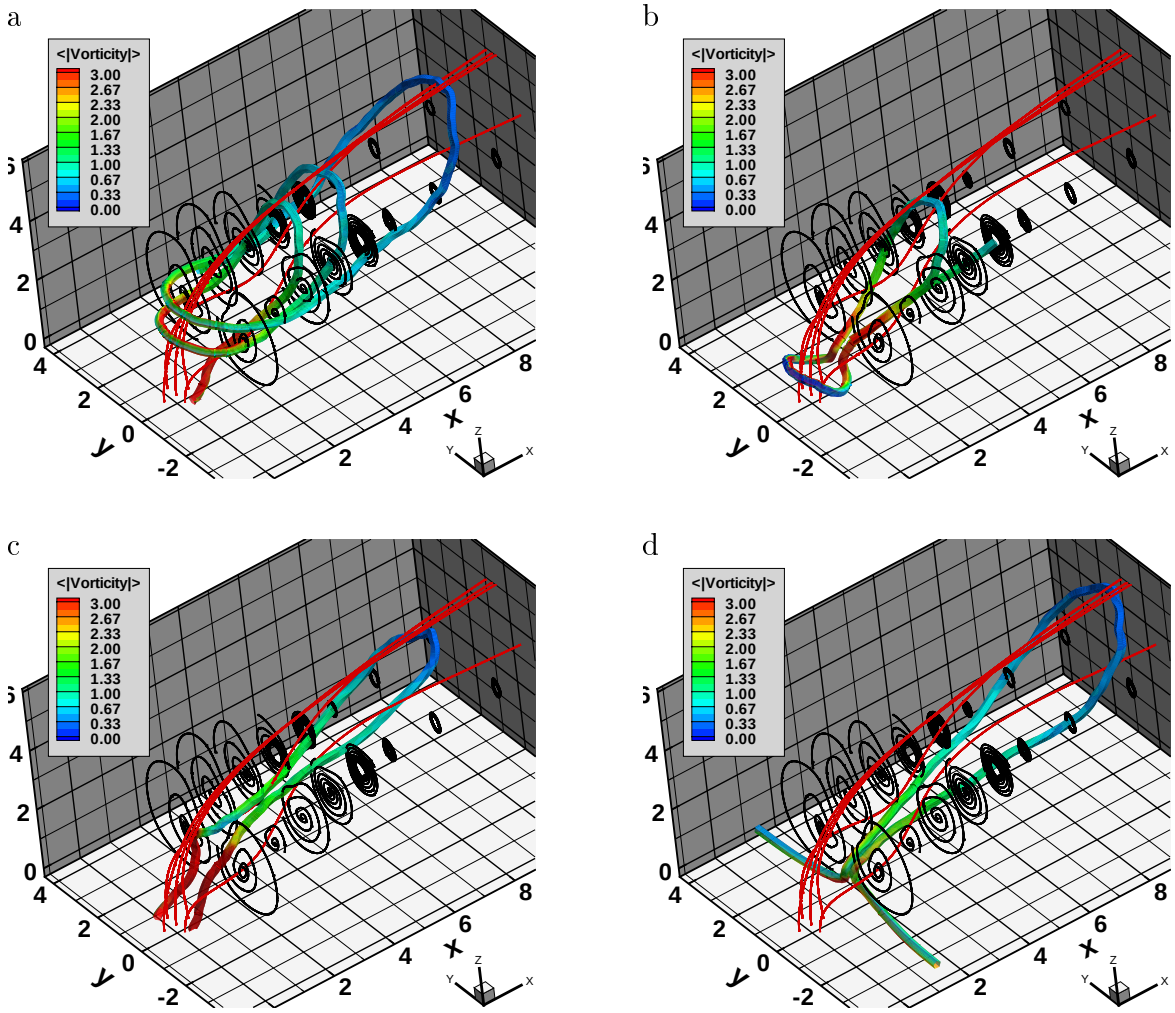

Figure 7: Average streamlines (red) and average vortex lines, coloured with the magnitude of the voticity vector. The black spirals are streamlines in planes perpendicular to the $x-$axis. The vortex lines have been calculated with different starting locations each time located in the center of one of the counter rotating vortices, i.e. close to the focus of the black spirals: a) starting in a focus at $x = 4.5D$, b) starting in a focus at $x = 5.54D$, c) starting in a focus at $x = 6.5D$, d) starting in a focus at $x = 8.0D$,

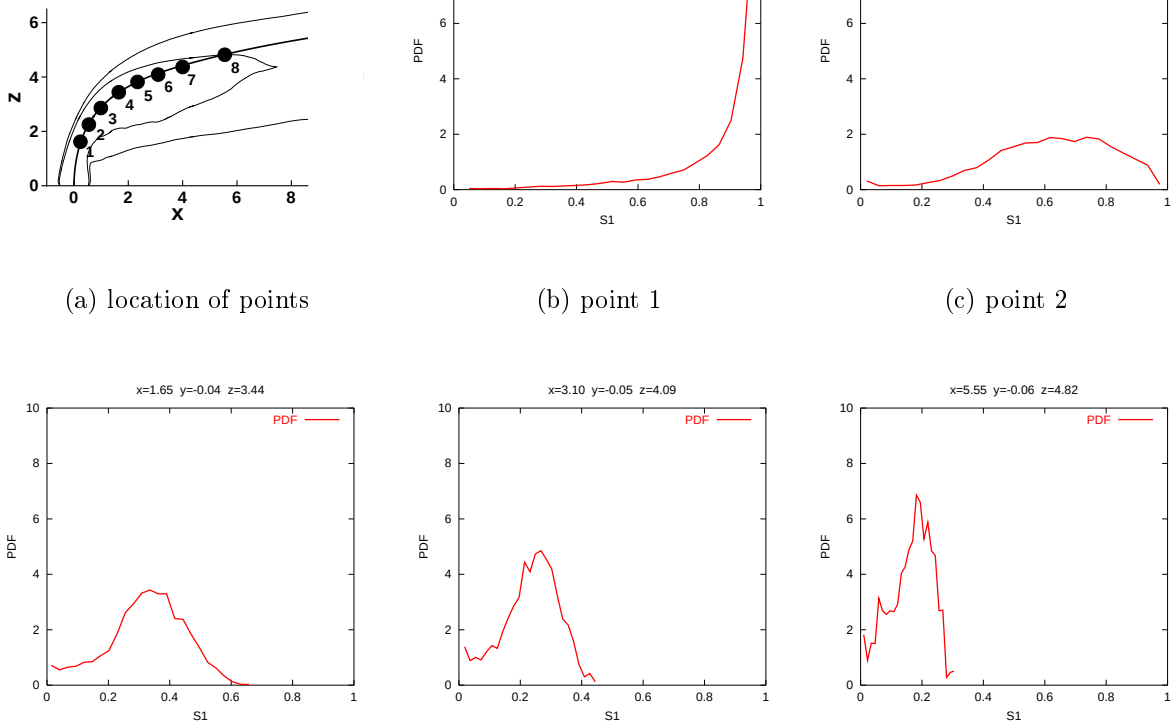

(a) location of points (b) point 1 (c) point 2

(d) point 4 (e) point 6 (f) point 8

Figure 8: PDF of the scalar concentration S_1 along the velocity trajectory of the jet at selected points along the central velocity trajectory of the jet as indicated in the sketch of picture (a). The thin lines display the levels $\langle S_1 \rangle = 0.05$ and $\langle S_1 \rangle = 0.2$ of the average concentration field.

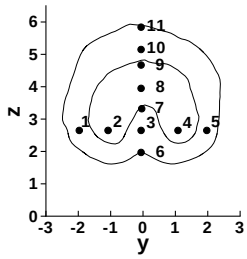

(a) location of points

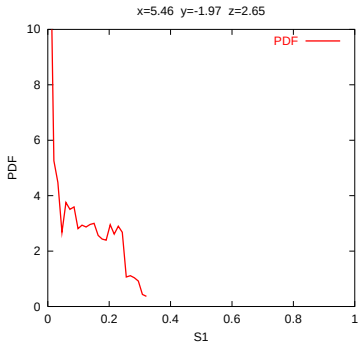

(b) point 1

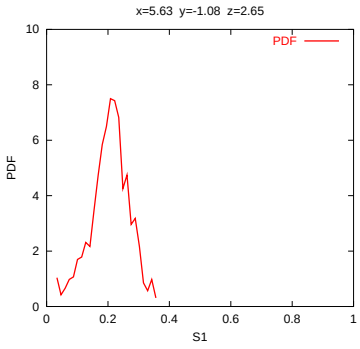

(c) point 2

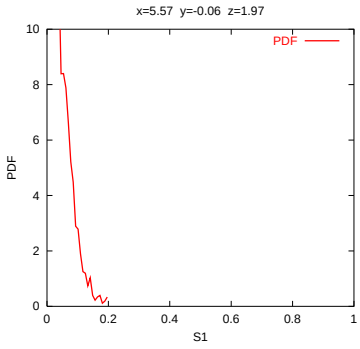

(d) point 6

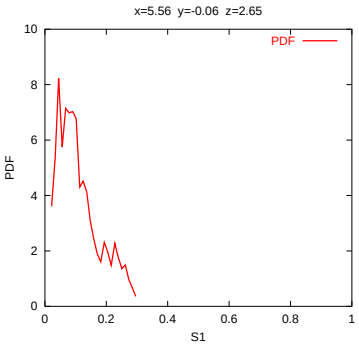

(e) point 3

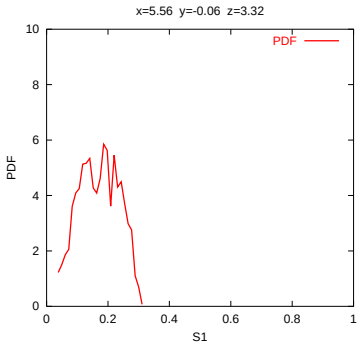

(f) point 7

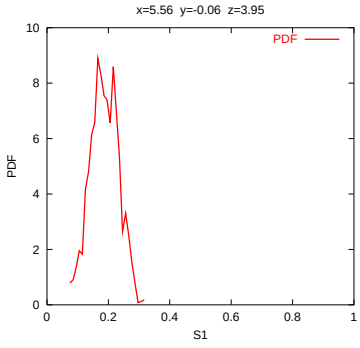

(g) point 8

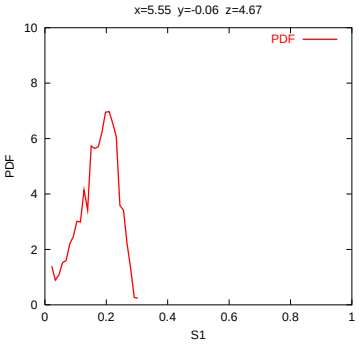

(h) point 9

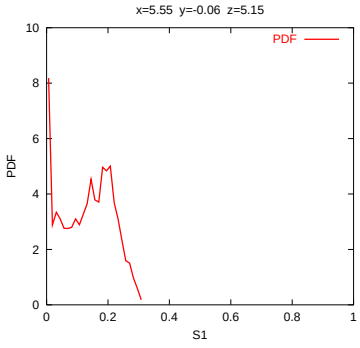

(i) point 10

Figure 9: PDF of the scalar concentration S_1 at selected points in a plane at $x = 5.54$ as sketched in picture (a). The thin lines display the levels $\langle S_1 \rangle = 0.05$ and $\langle S_1 \rangle = 0.2$ of the average concentration field.